Photoemission momentum mapping and wave function analysis of surface and bulk states on flat Cu(111) and stepped Cu(443) surfaces: A two-photon photoemission study

M. Hengsberger,[*] F. Baumberger,[†] H. J. Neff, T. Greber, and J. Osterwalder

Physik-Institut, Universität Zürich, Winterthurerstrasse 190, CH-8057 Zürich, Switzerland
(Received 10 September 2007; revised manuscript received 10 December 2007; published 21 February 2008)

Accurate momentum mapping of bulk and surface electronic states by angle-resolved two-photon photo-emission is demonstrated on Cu(111) and one of its vicinal surfaces, Cu(443), using laser light of 3.08 eV photon energy for excitation. The surface state dispersion found agrees well with that expected from the periodic arrangement of terraces and monatomic steps on Cu(443). Polarization dependent data suggest that the state consists of out-of-plane p_z orbitals like on the flat (111) copper surface, mixed with in-plane orbitals at the step edges. Maps of the Fermi surface taken from the vicinal surface are found to be in excellent agreement with conventional photoemission data and density-functional calculations. This proves that multiphoton photoemission can be used like direct one-photon photoemission as initial state spectroscopy with high energy and momentum resolution provided that no real intermediate states are involved in the excitation process.

PACS number(s): 73.20.At, 79.60.−i, 71.18.+y

I. INTRODUCTION

Angle-resolved photoemission spectroscopy (ARPES) measures the single particle spectral function $A(\epsilon, \vec{k})$ of solids and surfaces. This means that the photoelectron spectrum reflects the energy-momentum dispersion relation $\epsilon(\vec{k})$ modified by the many-body response of the system to the presence of the hole, i.e., the missing electron in the state characterized by $\epsilon(\vec{k})$. It has become a powerful technique for studying the electronic properties of solids in great detail.[1] Very recent developments include the use of quasicontinuous wave vuv lasers as excitation sources with photon energies as low as 6–7 eV, permitting solid state spectroscopy at the μeV scale[2–5] and with extremely high momentum resolution.[6] The theoretical foundation of ARPES is well developed[7] and it appears to be robust also at these lower photon energies.[6]

In contrast, two-photon photoemission (2PPE) is a more complicated process. Here, the absorption of a single photon is not sufficient to excite a photoelectron into the vacuum. Rather, a resonant or virtual excitation to an intermediate state is followed by the absorption of a second photon. Such processes occur with appreciable probability only in the extremely high photon densities of ultrashort laser pulses. In this coherent and time-dependent radiation field, the excitation and relaxation of intermediate and final states are determined by the optical Bloch equations.[8–10] The necessity for two-photon absorption opens the possibility to study the dynamics of the intermediate-state occupation on a femtosecond time scale by two-photon pump-probe experiments, where probe laser pulses are subject to a controlled femtosecond delay with respect to pump pulses. Hot electron dynamics on semiconductor[11] and metal surfaces[8,12,13] has been investigated by this method, including its spin dependence.[14,15] The most comprehensive studies have been carried out on image-potential states on metal surfaces, i.e., of electrons that are trapped just outside a metal surface by the Coulomb attraction by their image charge.[16–18]

While most of these studies to date have focused on the dynamics of surface states and image-potential states, 2PPE produces also spectral features from bulk electronic states.[19,20] In fact, the correct assignment of peaks in 2PPE to either surface or bulk origin, and whether it corresponds to an initial state or an intermediate state, is not a trivial matter. In principle, different scenarios can lead to a distinct peak in the 2PPE spectrum (see as well Ref. 21 and references therein).

(I) Nonresonant excitation from a well-defined occupied initial state of energy E_1 into a virtual intermediate state and subsequent excitation by the second photon into a photoemission final state (E_3). This process will lead to a peak in the 2PPE spectrum that is centered at the position $E_1 + 2h\nu$.[20] A similar peak would be measured in a regular ARPES experiment with a photon energy of $2h\nu$.[19]

(IIa) Resonant excitation from a well-defined initial state (E_1) into an intermediate state of energy E_2 and subsequent excitation into a final state (E_3). The resulting spectrum will show a very intense peak at position $E_2 + h\nu$. Detuning the photon energy from this resonance will maintain this relationship between peak position and photon energy because the second excitation step dominates the spectrum. At the same time, the peak intensity can drop by orders of magnitude from its value at resonance.[22]

(IIb) An intermediate state at energy E_2 can also be populated by indirect excitation mechanisms, i.e., by capturing hot electrons resulting from bulk excitations due to a first photon. The resulting peak will show the same photon-energy dependence as in case (IIa). The two mechanisms can be distinguished by their different dependence on the photon polarization.[10]

(III) Even in the absence of well-defined initial and intermediate states, peaks in the 2PPE spectrum can result from diffraction effects of the emitted electrons.[23] This mechanism applies for final states populated directly in the 2PPE process or indirectly by secondary electron cascades. The peaks are usually weak and rather broad and their positions do not depend on the photon energy.

Thus, the assignment of peaks and their dispersion to real states and their respective band structure relations is far from being straightforward and has to be corroborated by photon-
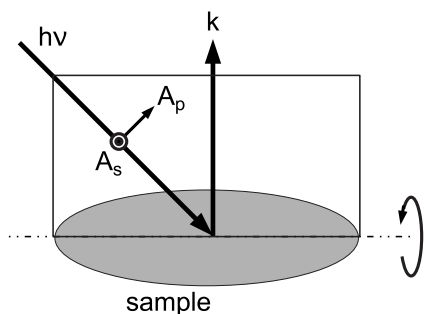
FIG. 1. Scheme of the geometry used in polarization dependent experiments: light incidence, optical surface normal, and direction of electron detection define the plane shown; light polarized within this plane is referred to as *p* polarization, and orthogonally polarized light as *s* polarization.

energy dependent measurements, for instance. Furthermore, as we will show in this work, the influence of final states is significant in the case of bulk bands. In this paper, we apply monochromatic angle-scanned 2PPE for band structure mapping of the occupied electronic structure on Cu(111) and Cu(443). The well characterized Cu(111) surface is investigated as a test case and is used to calibrate the spectrometer mapping function. Comparison with band structure calculations allow to identify a bulk direct transition and give an estimate of the perpendicular final state momentum.

II. EXPERIMENTAL SETUP

The spectra were taken in a modified Vacuum Generators ESCALAB 220 spectrometer described elsewhere.[24,25] In angle-resolving mode, the electron analyzer has an energy and an angle resolution of 30 meV and 1°, respectively, and the chamber is equipped with a computer-controlled two-axis sample goniometer that permits automatic scanning of all electron emission directions above the surface. A femtosecond laser system was used for 2PPE experiments. Laser pulses with 800 nm wavelength are generated in a commercial Ti:sapphire laser at a repetition rate of 76 MHz. The pulses are then frequency doubled in a 0.5 mm thick barium borate crystal and compressed to about 70 fs. The average power of the blue, frequency-doubled light is about 70 mW, corresponding to a pulse energy of ≈ 1 nJ.[25] An adjustable lens with 300 mm focal length mounted outside the photoemission ultrahigh vacuum chamber proved to focus sufficiently well to achieve count rates above 10 counts/s from the Cu(111) surface state. The combined energy resolution of the light and analyzer is estimated from the width of the surface state peak to be below 60 meV, mainly determined by the broad spectral width of the frequency-doubled femtosecond laser pulses (about 44 meV).

The light was incident under an angle of 45° from the electrostatic analyzer in a plane defined by the analyzer and the polar rotation axis of the sample, as shown in Fig. 1. The polarization of the light can be varied with a broadband polarization rotator to obtain linearly polarized light of arbitrary orientation or by using a $\lambda/4$ plate for circularly polarized light. The geometry and nomenclature used here are
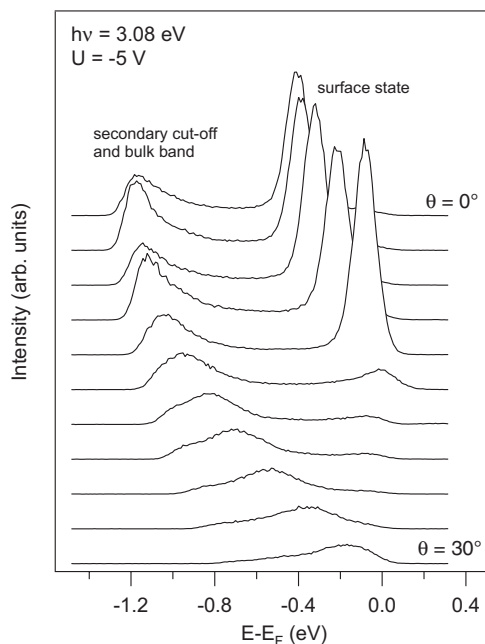

FIG. 2. 2PPE spectra from Cu(111) recorded at a temperature of 200 K with a photon energy of 3.08 eV. The spectra were measured at various polar emission angles, equidistantly spaced by 3° along the $[1\bar{1}2]$ azimuth. A bias voltage of −5 eV was applied to the sample; the ordinate refers to the initial state energy.

depicted in Fig. 1. However, the degree of polarization is limited by the complicated beam layout involving nonorthogonal deflections causing a phase shift of different polarization components upon reflections at dielectric mirrors. From the surface state data presented later on in this paper, we can give a lower bound of 97% for the degree of linear polarization.

The samples were prepared according to the recipes described in Ref. 26. Briefly, Ar sputtering at moderate energies (1 keV) was used followed by careful annealing up to about 525 K. Surface cleanliness and order were checked by x-ray photoelectron spectroscopy and low-energy-electron diffraction, respectively, and later on by monitoring the width and shape of the surface state peak under excitation with He I radiation. The work functions of the samples were 4.94 and 4.86 eV for the (111) and the (443) surface, respectively.

All experiments presented here have been performed with a photon energy of 3.08 eV at a sample temperature of 200 K. A bias voltage of −5 V was applied to the sample in order to avoid complications due to the vanishing transmission properties of the spectrometer at energies below the pass energy. The distortions of the electron trajectories resulting from the bias field will be treated in detail in the Appendix. The initial state energy with the Fermi level $E_F=0$ will be used as the energy scale throughout this paper except otherwise stated.

III. SURFACE STATE AS A REFERENCE

In Fig. 2, a set of energy distribution curves from Cu(111) is shown for various emission angles along $[\bar{1}\bar{1}2]$ (corre-
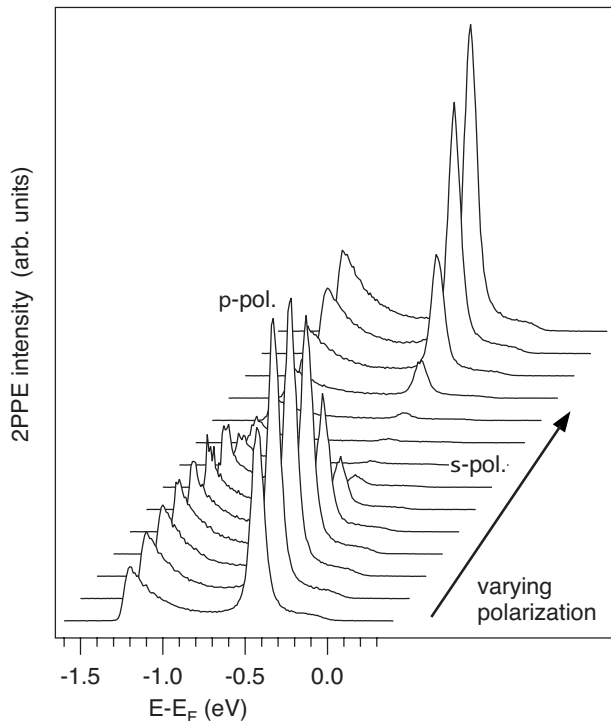
FIG. 3. Normal emission spectra from Cu(111) for varying orientations of the light polarization vector ($h\nu = 3.08$ eV): maximum intensity is observed for the polarization vector lying within the plane of incidence; the spectra are offset for the sake of clarity.
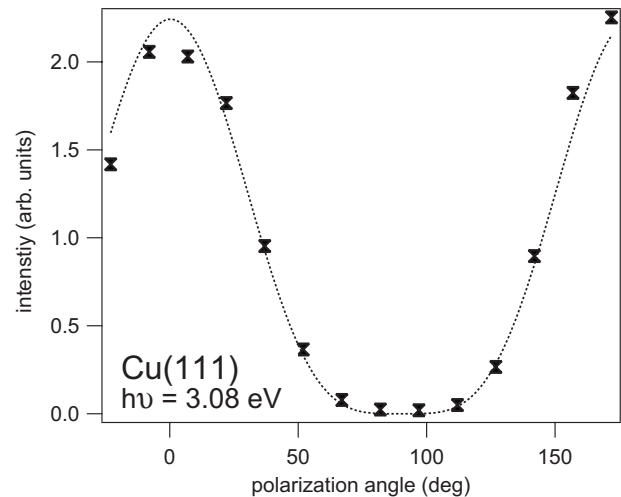

FIG. 4. Surface state intensity as a function of the angle between the polarization vector and surface normal (open diamonds) and fitting function (dotted line); the best fit is obtained by using the fourth power of a cosine function.

sponding to $\overline{\Gamma M}$ in the surface Brillouin zone). Cu(111) has no unoccupied surface state in normal emission and the first image-potential state is located 4.1 eV above E_F, close to the upper edge of the *sp*-band gap. Thus, with the photon energy of 3.08 eV, no long lived intermediate states are accessible and the photocurrent has to be assigned to *nonresonant* two-photon processes via a virtual state.[8] It is therefore straightforward to assign the dominant peak to two-photon transitions out of the Shockley surface state.

The assignment is corroborated by an analysis of the transition dipole, the orientation of which can be measured by rotating the linear light polarization, as shown in Fig. 3. Wolf *et al.* showed that in the case of linear light polarization, maximum photoemission intensity is to be expected with the polarization vector aligned with the transition dipole.[10] If the intermediate state is populated by direct excitation out of the initial state, the intensity should scale with the fourth power of the cosine of the angle between the polarization vector and transition dipole. The same holds true for the case of simultaneous absorption of two photons, i.e., a virtual intermediate state. In the case of an indirect excitation, i.e., a filling of the intermediate state by higher lying excited states,[10,27] the dependency should follow the square of the cosine. The surface state intensity extracted from the spectra presented in Fig. 3 is plotted in Fig. 4 against the angle of the polarization vector, zero corresponding to the vector potential lying within the plane of incidence (*p* polarization) with a maximum component along the surface normal (for the geometry see Fig. 1). It is obvious that the intensity scales with the fourth power of the cosine. Since no intermediate

states are available, the peak represents a two-photon excitation of the initial state, as outlined above. Moreover, the orientation of the transition dipole is found to be normal to the surface as expected for dipole transitions out of the Shockley surface state, the main orbital character of which is p_z, where z points out of the surface plane.

When determining dispersion relations, one has to be aware that spectra recorded with applied bias voltage U do not conserve the parallel momentum of the initial state.[25,28] The applied bias causes an electrostatic field above the sample, which bends the electron trajectories in a nontrivial way. To a first approximation, the field can be described by treating the analyzer entrance slit and sample as infinite planes lying on different potentials and including an angle which corresponds to the manipulator angle. In this case, the electron traces can approximately be described by a scaling law, the derivation of which will be described in detail in the Appendix. We obtain

$$k_{\parallel} = \frac{1}{\hbar}\sqrt{2mE_{kin}}\sin(\theta_m + \theta_x), \qquad (1)$$

where θ_x is the angular correction due to the bias field according to Eq. (A7) and θ_m, E_{kin}, and m denote the polar (manipulator) angle between the sample surface normal and analyzer axis, the photoelectron kinetic energy at the sample surface, and the free-electron mass, respectively.

In Fig. 5, a dispersion plot (A) and a 2PPE Fermi surface map (B) from Cu (111) are shown on a logarithmic gray scale as function of the emission angle. We find two strongly dispersing bands with concentric constant-energy contours for energies corresponding to the Fermi energy in the initial state. The outer circle corresponds to a cut through the neck of the bulk Fermi surface close to the L point of the bulk Brillouin zone and will be discussed in the next section. The inner circle is produced by photoelectrons out of the partially occupied Shockley surface state at the origin of the (111)
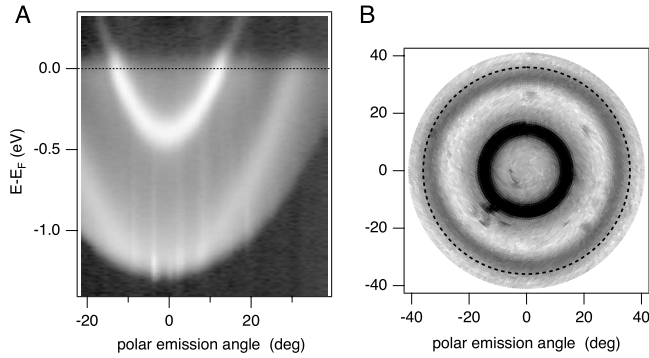
FIG. 5. (A) 2PPE dispersion plot and (B) Fermi surface map from Cu(111) recorded at 200 K with a photon energy of 3.08 eV as a function of emission angle. A bias voltage of −5 V was applied to the sample. In these plots, the photocurrent is displayed on a logarithmic gray scale; black corresponds to high intensity. The dashed circle in (B) serves as guide to the eyes in order to enhance the slight distortions of the contour of the bulk band.

surface Brillouin zone.[26] For a bias voltage of $U = -5$ V, we find the Fermi level transition of the surface state at $\pm 12.4°$. Invoking Eq. (1), this yields $k_F = 0.217$ Å^{-1}, which has to be compared to values determined with He I radiation to be between $k_F^{(111)} = 0.205$ (Ref. [26]) and 0.215 Å^{-1}.[29] Thus, the agreement is quite good despite the bias field applied in the case of the 2PPE experiment (see Appendix for a more detailed discussion).

IV. MOMENTUM MAPPING OF BULK BANDS

In the 2PPE dispersion plot in Fig. 5, a second free-electron-like band with the apex near $E_B = 1.2$ eV close to the vacuum cutoff and a Fermi level transition around $k_\parallel = 0.52$ Å^{-1} is observed. The transition cannot originate from surface-related features in the band structure. This is corroborated by the slight threefold symmetrical deformation (Fig. 5), which is reminiscent of the threefold rotational symmetry of the bulk [111] axis in Cu. To further clarify its origin, we performed density-functional calculations of the Cu bulk band structure, using the WIEN2K package.[30] The bands along the ΓL-symmetry line, which is perpendicular to (111), are shown in Fig. 6. Direct transitions with $E_3 - E_1 = 2h\nu$ are possible for $h\nu = 3.08$ eV at $k_{[111]} \approx 1.7$ Å^{-1}, close to the first L point [similar findings have been made on Ag(111) in Ref. [20]]. The initial state for this transition is sp-like, with $E_B = -1.56$ eV, in reasonable agreement with the experimental value. The final state band lies rather close to a free-electron band, in an inner potential of 12 eV, which is added in Fig. 6.

We thus expect in this case the free-electron final state approximation to be reasonably good and performed a band structure calculation along the k-space contour of a free electron in an inner potential of $V_i = 12$ eV, which represents a sphere for each final state energy E_f. The result is shown in Fig. 7, where the experimental Fermi surface is compared to the result of a bulk calculation for a constant momentum (radius in reciprocal space) of 1.86 Å^{-1}. In the calculation,
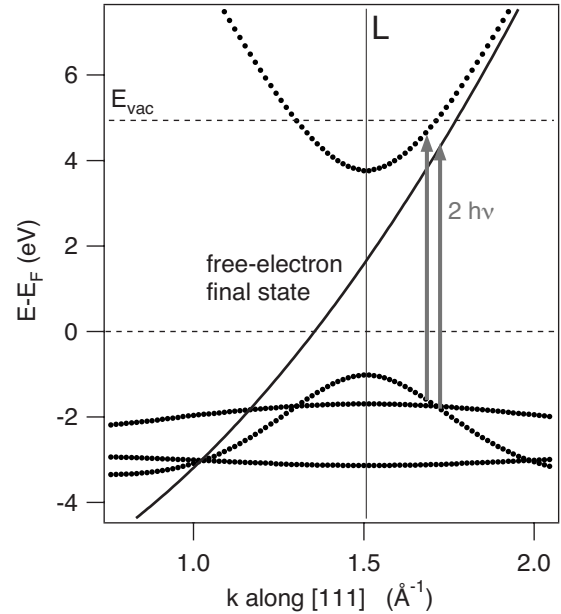

FIG. 6. Band structure along ΓL or [111] calculated with the DFT package WIEN2K (Ref. [30]) (dots). The arrows mark direct transitions with $2h\nu$ within the band structure and to a free-electron final state, added as a solid line. Note that the transition shown cannot be observed because the electron is not excited above the vacuum level E_{vac}.

the gray scale value is proportional to $E_f - E_i - 2h\nu$. Dark contours reflect thus small distances between initial and final state energies for these predefined wave vectors, i.e., momentum and energy are conserved at these locations. These are thus the locations where direct transitions occur. As expected from Fig. 6, we find a good agreement for initial states at the Fermi level.

Increasing deviations are observed, however, as the final state wave vector approaches the L point. This is visualized in Fig. 8: assuming a roughly isotropic parabolic dispersion of the final state band around the L point,[31] the bulk initial state cannot contribute to the photoemission spectra around
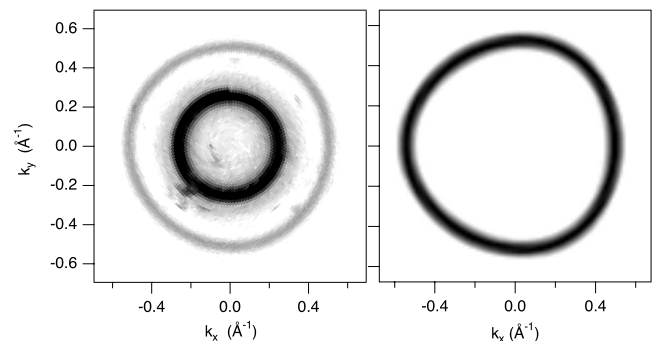

FIG. 7. Comparison of experimental and theoretical bulk Fermi surface. Left panel: experimental 2PPE Fermi surface map from Fig. 5 vs momentum $k_\parallel$; here, x refers to the bulk [$1\bar{1}2$] direction or the ΓLUX plane. Right panel: intersection of a final state sphere of $k_f = 1.86$ Å^{-1} with bulk initial states as calculated with the DFT package WIEN2K (Ref. [30]) the calculation only reproduces bulk states.
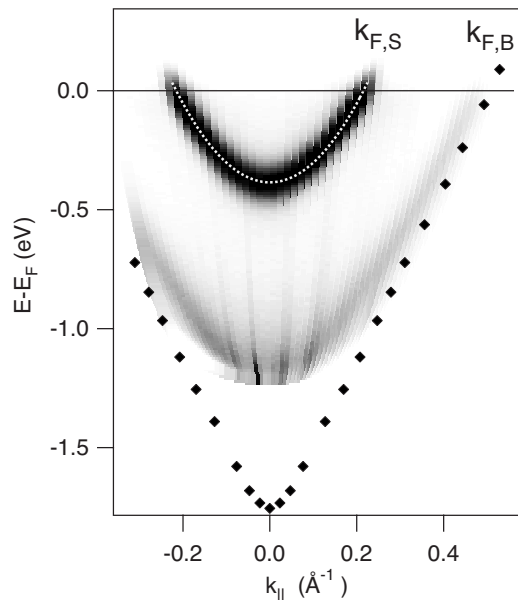
FIG. 8. 2PPE data from Fig. 5 vs momentum parallel to the surface within the bulk ΓLUX plane on a linear gray scale together with the known dispersion of the surface state (dotted white line) and bulk transitions calculated with the DFT package WIEN2K (Ref. 30) (solid diamonds); $k_{F,S}$ and $k_{F,B}$ denote the Fermi momenta of surface and bulk bands, respectively.

normal emission due to the low photon energy. On the other hand, the closer the free-electron final state mimics the upper bulk band, the better is the agreement between the experimental dispersion and the band structure of the initial states. We thus conclude that the kinematics of monochromatic 2PPE are well described by direct transitions in three-dimensional k space with $E_f - E_i = 2h\nu$. The free-electron final state approximation might be made in favorable cases but is not generally applicable.

V. DISPERSION ON THE VICINAL SURFACE

Clear advantages arising from the laser excitation over more conventional high-energy light sources are the small spot size and defined polarization, and the low energy, yielding an expanded k scale and final state momenta close to the L point. Vicinal surfaces, cut at a small and well-defined angle from a low-Miller-index plane, exhibit a regular array of terraces separated by usually monatomic steps (see, e.g., Refs. 26 and 32 and references therein). The corresponding surface Brillouin zones are small, necessitating a high momentum resolution for studies of electronic states confined by the potential barriers at the step edges.[33,34]

In Fig. 9, a 2PPE Fermi surface map from Cu(443), a vicinal to Cu(111), is shown together with a dispersion plot perpendicular to the steps of this vicinal surface. The data sets show three different bands: the surface state band labeled S, centered at $k_x \approx 0.19$ Å^{-1}, a downstairs umklapp of this band (labeled SU),[33] and, last, the bulk sp-band B as found on Cu(111). The nonconcentric appearance of the sp band and surface state Fermi surface is a consequence of $k_\parallel$ conservation. The momentum shift of the surface state is
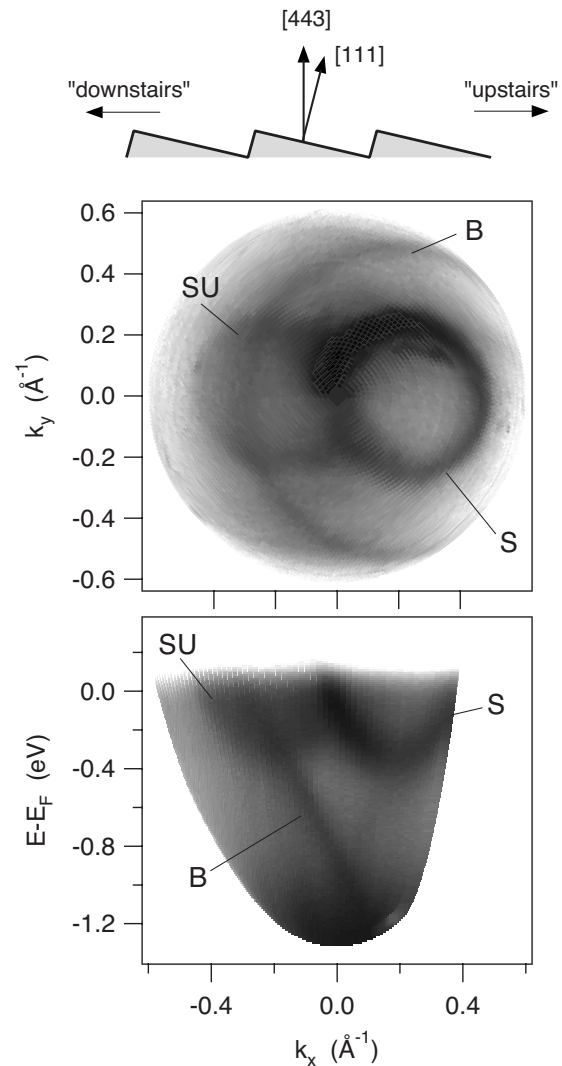

FIG. 9. Angle-scanned 2PPE data from Cu(443) recorded at 200 K with a photon energy of 3.08 eV. Top panel: Fermi surface map shown on a logarithmic gray scale; bottom panel: dispersion plot. The data are shown on a logarithmic intensity scale; black corresponds to a high intensity. The three observed dispersing bands are annotated as S (surface state), SU (surface state umklapp), and B (bulk band).

given by the surface projection of the L point, independent of photon energy indicating a surface state extending over several terraces.[26,32] For bulk transitions, on the other hand, features appearing on the flat surface in normal emission shift on a vicinal surface by $\Delta k_x = k_f \sin \alpha$, where $\alpha = 7.33°$ is the miscut angle.[35] The center of the sp-band Fermi level transition is thus expected at $k_x \approx 0.24$ Å^{-1}, slightly different from the center of the surface state, consistent with the experiment.

The surface state umklapp seen in Fig. 9 is observed only on the left-hand side of the fundamental band, i.e., for reciprocal lattice vectors pointing downstairs. Different umklapp intensities for ascending and descending reciprocal lattice vectors are typical for the free-electron-like surface states on vicinal noble metal surfaces[36] and can generally be described with the proportionality of the matrix element to the initial

state wave function. In k space, the initial state wave function shows a Lorentzian distribution of wave vectors $k_\perp$ around the L points of the bulk Brillouin zones in the extended zone scheme. Varying $k_{f\perp}$ with the photon energy, wave functions centered at different L points can be sampled. For surface states with a short enough decay length in real space, k_z extends over more than one Brillouin zone and, close to a Γ point, surface state wave functions from two consecutive L points can be probed simultaneously.[36]

However, in the present case, the final state momentum is 1.86 Å^{-1}, as determined from the bulk direct transitions (Fig. 6) and therefore close to the L point, where one expects strong intensity of the main peak but vanishing spectral weight in the umklapp bands. Even if we allowed for very large broadening of the final and initial state momenta perpendicular to the surface, the umklapp would be expected in the opposite direction, i.e., for momenta pointing toward the projection of $L_{3/2\ 3/2\ 3/2}$ onto the surface plane, rather than $L_{1/2\ 1/2\ 1/2}$ where the umklapp band is actually observed. The expected behavior was recently found to correctly describe photoemission spectra from Cu(443) taken at soft x-ray energies between 20 and 90 eV,[37] and the appearance of the umklapp band at low energy close to the L point is somewhat surprising. This indicates that the assumption of a free-electron final state might be oversimplified. In order to check for possible band structure effects in the final state, we calculated the *bulk* energy bands with density-functional theory (DFT) along lines perpendicular to the surface, for k_x values of the main surface state band, and umklapp bands in both directions like in Fig. 6. Possible $k_{f\perp}$ values are then found as $k_z(2h\nu - E_B)$, similar to the method used in Fig. 6. This procedure reveals no significant deviation from $k_{f\perp}$ of a free-electron final state, thus excluding final state band structure effects as the reason for the direction dependent umklapp intensity. Alternative scenarios should include a realistic description of intermediate and final states, which is beyond the scope of this work. Strong intensity variations of the spots in low-energy-electron diffraction (LEED) with energy indeed suggest that a treatment of the final state as time-reversed LEED state might explain the strong intensity difference of the umklapp processes for different directions and between soft x-ray and 2PPE energies. In contrast to that, the absence of an umklapp band for the bulk state suggests that the effect might be due to the initial state effect. A conclusive answer, however, has to await new measurements closing the gap in photon energy between x rays and laser light.

Finally, the photoemission intensity out of the surface state on Cu(443) has been measured in normal emission as a function of angle between light polarization and the plane of incidence. The latter is spanned by the step edges and the normal of the optical surface in the case of the vicinal sample. Due to the orbital character of the surface state, maximum intensity is expected to occur for the polarization vector being normal to the (111)-oriented terraces, i.e., at an angle corresponding to the nominal miscut of 7.33° of the surface.

In our experiment, the sample orientation and the detection in normal emission were kept constant, while the polarization vector of the light was rotated. The intensity as recorded as function of the angle between the polarization
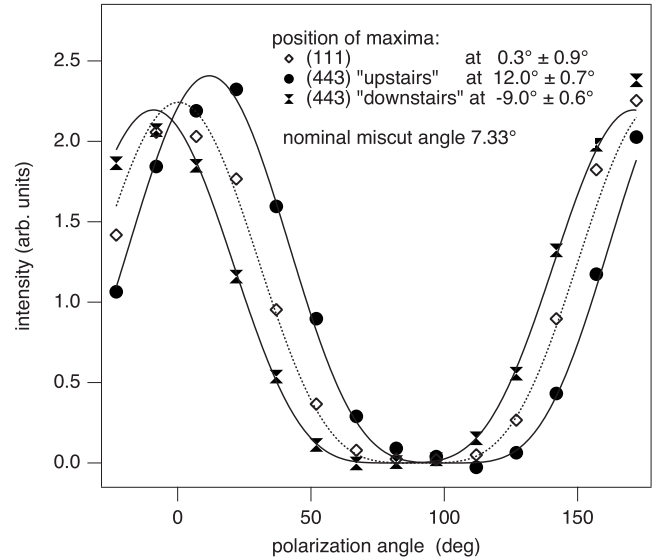

FIG. 10. Same plot as in Fig. 4 but including data taken from the vicinal surface: the surface state intensity clearly exhibits a $\cos^4$ behavior as a function of angle between the polarization vector and the plane of incidence. In this case, the plane of incidence was oriented parallel to the step edges such that the (111) terraces include the nominal miscut angle with the plane of incidence. The measurements were effectuated for the "upstairs" direction corresponding to the left and once to the right of the plane of incidence. The angles of maximum intensity are given for the three orientations.

vector and the surface normal is plotted in Fig. 10 together with the measurement for the flat (111) surface for the same orientation of the *optical* surface of the sample, i.e., normal emission. Owing to the low symmetry of the vicinal surface, the angle corresponding to a precise p polarization is obtained by rotating the vicinal surface around the normal by 180° and by taking the same data set for the second orientation, in which the terraces are flipped with respect to the plane of light incidence. As can be seen from Fig. 10, the difference in angle of the maxima for the two orientations of the vicinal surface is found to be 21°, thus significantly higher than twice the nominal miscut angle of about 7.3°. The deviation of about 3° gives evidence for a slight rotation of the transition dipole toward the terrace planes and, thereby, to a significant contribution of in-plane orbitals to the wave function, which is likely to arise at the step edges where due to the reduced coordination the wave function is altered. This is in full agreement with recent calculations of photoemission spectra from vicinal surfaces:[38] the authors claim that the wave function of the surface state is strongly mixed with bulk states of s and d characters for momenta close to the boundary of the surface Brillouin zone. For measurements close to normal emission, a weaker but nevertheless observable mixing would be expected. Indeed, our measurements suggest that the wave function of the initial state is tilted toward the "upstairs" direction due to mixing with bulk states at the step edges.

VI. CONCLUSION

In conclusion, we have demonstrated that band mapping of surface and bulk states is possible at low photon energies

and even by means of multiphoton spectroscopy, provided that no resonant intermediate state alters the observed peak dispersion. At least for bulk states, final state effects have to be taken into account. Close to the Fermi energy, the agreement between experiment and numerical DFT band structure calculations was found to be very satisfactory in the case of copper because the final bands are close to behaving like free electrons. Due to experimental difficulties encountered at low photon energies, effects of electrostatic fields have to be considered which may distort the mapping function of the spectrometer. Using a simple formalism, however, most of these effects can numerically be modeled, allowing the mapping function to be reestablished to an overall accuracy in the percent range in momentum. As has been shown recently, many-particle concepts like spectral function may still be used at these energy levels, which together with the present findings opens new possibilities for studying the electronic structure of solids with unprecedented energy and time resolution and the full mapping capabilities of angle-resolved photoemission.

ACKNOWLEDGMENT

APPENDIX: A SIMPLE MODEL FOR MOMENTUM MAPPING IN ELECTROSTATIC FIELDS

It is the purpose of this section to show how one may, based on a simple model, derive a formula allowing the momentum component parallel to the surface to be calculated even in the presence of a static electric field. Such a field is provided by the work function difference between the entrance electrode of the analyzer and the sample or else by an additional bias voltage applied to the sample. In practice, such fields should be avoided in the case of time-of-flight spectrometers, e.g., by compensating a difference in work function by an appropriate bias voltage. However, a bias acceleration voltage is often used in conjunction with electrostatic analyzers in order to avoid the low-energy, low-transmission range of the electron-optical system, like in the present case. The geometry underlying the model is shown in Fig. 11.

For the calculation, the entrance aperture of the analyzer and the sample surface are replaced by two (infinite) planes which intersect in a line, the position of which depends on the polar angle of the sample. The latter is referred to hereafter as the manipulator angle θ_m. The analyzer is supposed to accept electrons entering the electrostatic lens in a negligibly small solid angle around its symmetry axis, which is indicated in Fig. 11.

Starting from the coordinate system given in Fig. 11, we solve the equations of motion of the photoemitted electrons, which we write as
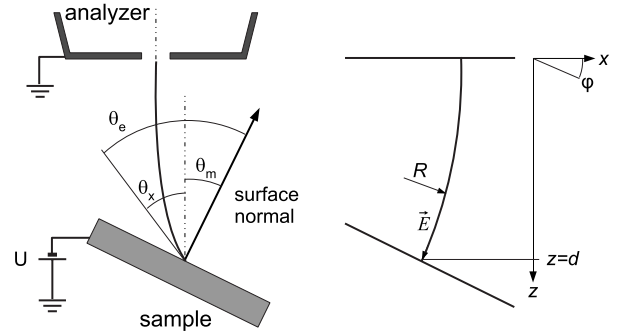
$$d\dot{z}^2 = 2\ddot{z}dz, \tag{A1a}$$

FIG. 11. The experimental geometry: in the calculation, a simplified model was used replacing the sample and the analyzer entrance by two infinite planes mutually intersecting under the manipulator angle θ_m; θ_m, the sample bias U, and the kinetic energy are input parameters and the electron emission angle θ_e is the result of the calculation. On the right-hand side, the coordinate system $\{x|z\}$ is plotted along with some variables and dimensions used in the calculations.

$$d\dot{x} = \ddot{x}dz/\dot{z}. \tag{A1b}$$

The third coordinate, y, is neglected and the initial coordinates $x=0$ and $z=d$ correspond to the starting point of the trajectory. The initial conditions are given by the kinetic energy of the photoelectron and by the true emission angle. At the entrance of the analyzer, the electron has a different speed due to the stationary bias field and the final direction of propagation of the electron is along the analyzer axis, i.e., $\dot{x}=0$ for $z<0$. The acceleration is given for any value of z by the strength and angle of the electric field. The latter is modeled by a field with circular field lines

$$\vec{E} = \begin{bmatrix} -E\sin\phi \\ 0 \\ E\cos\phi \end{bmatrix}, \tag{A2}$$

where

$$\sin\phi = \frac{z}{R} = \frac{z\theta_m}{l}.$$

The strength of the field, E, is then given by $E=U/l$, where $l=R\theta_m$ denotes the length of a field line. Combining Equations (A1a) and (A2) yields

$$d\dot{z}^2 = \frac{2eE}{m}\sqrt{1 - \left(\frac{\theta_m z}{l}\right)^2} dz, \tag{A3}$$

which can easily be integrated. The result is

$$v_z^2(z=0) - v_z^2(z=d) = \frac{eU}{m}\left[\sqrt{1 - \theta_m^2} + \frac{\arcsin\theta_m}{\theta_m}\right]. \tag{A4}$$

Due to the following relations:

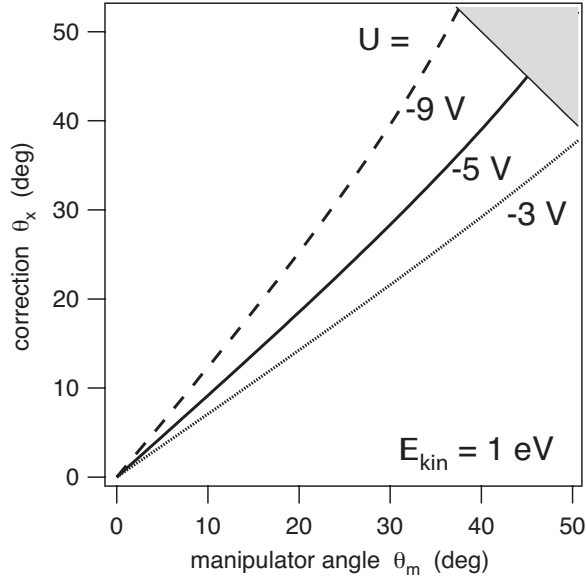$$v_z^2(0) = \frac{\hbar^2 k^2(0)}{m^2} = \frac{2}{m}(E_{kin} - eU), \tag{A5a}$$

FIG. 12. Plot of the correction of the emission angle versus the nominal (manipulator) angle for bias voltages of −3, −5, and −9 V and a kinetic energy of 1 eV; the gray shaded area in the upper right part of the plot visualizes the condition that the emission angle never exceeds 90°.

$$v_z^2(d) = v^2(d)\cos^2 \theta_x = \frac{2}{m}\cos^2 \theta_x\, E_{kin}, \quad (A5b)$$

the angular correction θ_x, which is defined by the difference between the real emission angle and the manipulator angle $\theta_x = \theta_e - \theta_m$, is finally given by

$$\sin \theta_x = \left(\frac{eU}{E_{kin}} \left[1 - \frac{\sqrt{1 - \theta_m^2}}{2} - \frac{\arcsin \theta_m}{2\theta_m} \right] \right)^{1/2}. \quad (A6)$$

For the sake of completeness, the analytic solution of the more simple model problem invoking another approximation, in which the curved electric field line in Fig. 11 is replaced by a straight one, is given here,

$$\tan \theta_x = \left[\frac{eU(1 - \sin \theta_m / \theta_m)}{E_{kin} - eU(1 - \sin \theta_m / \theta_m)} \right]^{1/2}. \quad (A7)$$

Its derivation is similar to the one presented above and the relative error is less than 1% for manipulator angles below about 15°, increasing progressively to about 5% at emission angles around 30°.

The correction according to Eq. (A6) and (A7) vanishes, as required for small bias voltage and manipulator angle. The difference between both results is negligible for real experimental situations around normal emission, the latter [Eq. (A7)] being more handy to use. The correction angle as calculated using Eq. (A7) is plotted in Fig. 12 versus the setting of the manipulator angle for typical bias voltages and an electron kinetic energy of 1 eV directly at the sample. As can be seen in Fig. 12, the corrections are important and should never be neglected in cases where highly accurate band mapping is required.
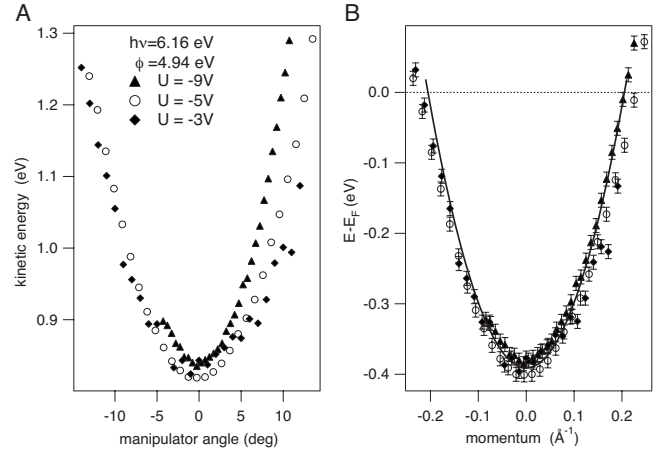

FIG. 13. Comparison of the experimental dispersion obtained by employing various bias voltages. (A) Raw peak positions on the kinetic energy scale vs the manipulator angle; data sets for bias voltages of −3 V (solid diamonds), −5 V (open circles), and −9 V (solid triangles) are shown. (B) Same data plotted against the momentum calculated using Eq. (A7) including the work function difference between the sample and analyzer; the solid line represents the surface state dispersion as measured on the same sample using He I radiation.

In order to estimate the mapping error, measurements of the surface state dispersion of the Cu(111) surface state have been performed for various bias voltages. Three representative data sets are shown in Fig. 13(a). Using a proper Fermi energy reference (e.g., spectra from polycrystalline silver) and utilizing the formula given by Eq. (A7), the $E(k)$-dispersion curves in Fig. 13 are obtained. The results are summarized in Table I.

As can be seen from Table I, the errors obtained from a single data set underestimate the true absolute error. The direct comparison with conventional photoemission data reveals that the general agreement is satisfactory but that, in particular, effective band masses are overestimated. This,

TABLE I. Comparison of maximum binding energy E_0, effective band mass $m^\star$, and Fermi wave vector k_F obtained for the Cu(111) surface state by means of 2PPE and high-resolution photoemission. (Errors are given as standard deviations.)

Bias[a]	$E_0 - E_F$ (eV)	$m^\star$ (m_0)[b]	k_F (Å^{-1})
−3[c]	−0.385 ± 0.003	0.465 ± 0.019	0.217 ± 0.009
−5[c]	−0.399 ± 0.001	0.458 ± 0.003	0.219 ± 0.002
−9[c]	−0.378 ± 0.001	0.436 ± 0.004	0.208 ± 0.002
all[d]	−0.387 ± 0.01	0.453 ± 0.015	0.215 ± 0.006
0[e]	−0.399 ± 0.003	0.41 ± 0.02	0.205
0[f]	−0.435 ± 0.001	0.412	0.215

[a]Excluding the work function difference.
[b]Free-electron rest mass.
[c]2PPE (this work).
[d]Mean values and errors of all 2PPE results obtained in this work.
[e]HR-PES (Ref. 26); data taken from the same sample.
[f]HR-PES (Ref. 29); data taken at low temperature (Ref. 39).

however, might be a consequence of the moderate energy resolution encountered in 2PPE, which is known to broaden and shift maxima in photoemission spectra in the sense of the dispersion and, thereby, mimic a heavier band. Furthermore, within the mathematical treatment of this simple model, some approximations have been made. The corresponding total error of the momentum scale is of the order of 1% as shown above and scales quadratically with the manipulator angle for realistic conditions. The largest error, however, is generated by the physical model, in which the sample was approximated by an infinite plane. The exact trajectories of the photoelectrons will depend on the exact shape of the sample holder and analyzer entrance. Ray tracing calculations with SIMION[40] show that $k_\parallel$ is even in the complicated experimental geometry reasonably well proportional to $\sin\theta$. However, the proportionality constant depends on the experimental setup. It is interesting to note that already a work function difference of 0.5 eV between a sample of 7 mm diameter and the surrounding sample holder can bend trajectories by more than 2° at a polar emission angle of 30°. We thus conclude that a more accurate $k_\parallel$ mapping at very low kinetic energies requires in standard experimental setups a calibration with a well known dispersion curve, as provided, e.g., by the Shockley surface state on Cu(111).

*matthias@physik.uzh.ch

†Present address: School of Physics and Astronomy, University of St. Andrews North Haugh, St. Andrews, Fife, KY16 9SS, UK.

1 S. Hüfner, S. Schmidt, and F. Reinert, Nucl. Instrum. Methods Phys. Res. A **547**, 8 (2005).

2 T. Kiss, F. Kanetaka, T. Yokoya, T. Shimojima, K. Kanai, S. Shin, Y. Onuki, T. Togashi, C. Zhang, C. T. Chen, and S. Watanabe, Phys. Rev. Lett. **94**, 057001 (2005).

3 T. Kiss, T. Shimojima, F. Kanetaka, K. Kanai, T. Yokoya, S. Shin, Y. Onuki, T. Togashi, C. Q. Zhang, C. T. Chen, and S. Watanabe, J. Electron Spectrosc. Relat. Phenom. **144-147**, 953 (2005).

4 K. Ishizaka, T. Kiss, T. Shimojima, T. Yokoya, T. Togashi, S. Watanabe, C. Q. Zhang, C. T. Chen, Y. Onose, Y. Tokura, and S. Shin, Phys. Rev. B **72**, 233202 (2005).

5 K. Ishizaka, R. Eguchi, S. Tsuda, T. Yokoya, A. Chainani, T. Kiss, T. Shimojima, T. Togashi, S. Watanabe, C.-T. Chen, C. Q. Zhang, Y. Takano, M. Nagao, I. Sakaguchi, T. Takenouchi, H. Kawarada, and S. Shin, Phys. Rev. Lett. **98**, 047003 (2007).

6 J. D. Koralek, J. F. Douglas, N. C. Plumb, Z. Sun, A. V. Federov, M. M. Murnane, H. C. Kapteyn, S. T. Cundiff, Y. Aiura, K. Oka, H. Eisaki, and D. S. Dessau, Phys. Rev. Lett. **96**, 017005 (2006).

7 S. Hüfner, *Photoelectron Spectroscopy*, 3rd ed. (Springer, Berlin, 2003).

8 T. Hertel, E. Knoesel, M. Wolf, and G. Ertl, Phys. Rev. Lett. **76**, 535 (1996).

9 M. J. Weida, S. Ogawa, H. Nagano, and H. Petek, J. Opt. Soc. Am. B **17**, 1443 (2000).

10 M. Wolf, A. Hotzel, E. Knoesel, and D. Velic, Phys. Rev. B **59**, 5926 (1999).

11 J. Bokor, R. Storz, R. R. Freeman, and P. H. Bucksbaum, Phys. Rev. Lett. **57**, 881 (1986).

12 M. Aeschlimann, S. Pawlik, and M. Bauer, Ber. Bunsenges. Phys. Chem. **99**, 1504 (1995).

13 U. Bovensiepen, J. Phys.: Condens. Matter **19**, 083201 (2007).

14 M. Aeschlimann, M. Bauer, S. Pawlik, W. Weber, R. Burgermeister, D. Oberli, and H. C. Siegmann, Phys. Rev. Lett. **79**, 5158 (1997).

15 A. B. Schmidt, M. Pickel, M. Wiemhofer, M. Donath, and M. Weinelt, Phys. Rev. Lett. **95**, 107402 (2005).

16 K. Giesen, F. Hage, F. J. Himpsel, H. J. Riess, and W. Steinmann, Phys. Rev. Lett. **55**, 300 (1985).

17 T. Fauster and M. Weinelt, J. Electron Spectrosc. Relat. Phenom. **114-116**, 269 (2001).

18 U. Höfer, I. L. Shumay, Ch. Reuss, U. Thomann, W. Wallauer, and Th. Fauster, Science **277**, 1480 (1997).

19 S. Pawlik, R. Burgermeister, M. Bauer, and M. Aeschlimann, Surf. Sci. **402-404**, 556 (1998).

20 N. Pontius, V. Sametoglu, and H. Petek, Phys. Rev. B **72**, 115105 (2005).

21 W. Steinmann, Appl. Phys. A: Solids Surf. **49**, 365 (1989).

22 K. Giesen, F. Hage, F. J. Himpsel, H. J. Riess, and W. Steinmann, Phys. Rev. B **33**, 5241 (1986).

23 M. Bovet, V. N. Strocov, F. Clerc, C. Koitzsch, D. Naumovic, and P. Aebi, Phys. Rev. Lett. **93**, 107601 (2004).

24 T. Greber, O. Raetzo, T. J. Kreutz, P. Schwaller, W. Deichmann, E. Wetli, and J. Osterwalder, Rev. Sci. Instrum. **68**, 4549 (1997).

25 M. Muntwiler, M. Hengsberger, A. Dolocan, H. J. Neff, T. Greber, and J. Osterwalder, Phys. Rev. B **75**, 075407 (2007).

26 F. Baumberger, T. Greber, and J. Osterwalder, Phys. Rev. B **64**, 195411 (2001).

27 G. Ferrini, C. Giannetti, G. Galimberti, S. Pagliara, D. Fausti, F. Banfi, and F. Parmigiani, Phys. Rev. Lett. **92**, 256802 (2004).

28 M. Rohleder, K. Duncker, W. Berthold, J. Güdde, and U. Höfer, New J. Phys. **7**, 103 (2005).

29 F. Reinert, G. Nicolay, S. Schmidt, D. Ehm, and S. Hüfner, Phys. Rev. B **63**, 115415 (2001).

30 K. Schwarz, P. Blaha, and G. K. H. Madsen, Comput. Phys. Commun. **147**, 71 (2002).

31 H. Eckart, L. Fritsche, and J. Noffke, J. Phys. F: Met. Phys. **14**, 97 (1984).

32 M. Hengsberger, D. Purdie, M. Garnier, K. Breuer, and Y. Baer, Surf. Sci. Lett. **405**, L 491 (1998).

33 F. Baumberger, M. Hengsberger, M. Muntwiler, M. Shi, J. Krempasky, L. Patthey, J. Osterwalder, and T. Greber, Phys. Rev. Lett. **92**, 016803 (2004).

34 F. Baumberger, T. Greber, and J. Osterwalder, Phys. Rev. B **62**, 15431 (2000).

35 R. Matzdorf, Surf. Sci. Rep. **30**, 153 (1998).

36 J. E. Ortega, A. Mugarza, V. Repain, S. Rousset, V. Pérez-Dieste, and A. Mascaraque, Phys. Rev. B **65**, 165413 (2002).

37 F. Baumberger, M. Hengsberger, M. Muntwiler, M. Shi, J. Krempasky, L. Patthey, J. Osterwalder, and T. Greber, Phys. Rev. Lett. **92**, 196805 (2004).

[38] R. Eder and H. Winter, Phys. Rev. B **70**, 085413 (2004).

[39] Note that the binding energy of the Shockley surface state is temperature dependent. The data from Ref. 29 were taken at low temperature where the binding energy increases by about 40 meV; see R. Panagio, R. Matzdorf, G. Meister, and A. Goldmann, Surf. Sci. **336**, 113 (1995).

[40] SIMION software package, Idaho National Labs (http://www.simion. com/).